

The extreme mass transfer and high magnetic field of the first ultraluminous pulsar M82 X-2

Matteo Bachetti,^{1*} Marianne Heida,² Thomas Maccarone,³ Daniela Huppenkothen,⁴
 Gian Luca Israel,⁵, Didier Barret,⁶ Murray Brightman,⁷, McKinley Brumback,⁷
 Hannah P. Earnshaw,⁷ Karl Forster,⁷ Felix Fürst,⁸ Brian W. Grefenstette,⁷
 Fiona A. Harrison,⁷ Amruta D. Jaodand,⁷ Kristin K. Madsen,⁹ Matthew Middleton,¹⁰
 Sean N. Pike,⁷ Maura Pilia,¹ Juri Poutanen,^{11,12,13} Daniel Stern,⁷
 John A. Tomsick,¹⁴ Dominic J. Walton,^{15,16} Natalie Webb,⁶ Jörn Wilms¹⁷

¹INAF-Osservatorio Astronomico di Cagliari, via della Scienza 5, I-09047 Selargius (CA), Italy

²European Southern Observatory, Karl-Schwarzschild-Strasse 2, 85748 Garching bei München, Germany

³Department of Physics and Astronomy, Texas Tech University, Lubbock, TX, USA

⁴SRON Netherlands Institute for Space Research, Sorbonnelaan 2, 3584 CA, Utrecht, Netherlands

⁵INAF-Osservatorio Astronomico di Roma, via Frascati 33, I-00078 Monteporzio Catone, Italy

⁶IRAP, Université de Toulouse, CNRS, CNES, 9 avenue du Colonel Roche, 31028, Toulouse, France

⁷Cahill Center for Astronomy and Astrophysics, California Institute of Technology, Pasadena, CA 91125, USA

⁸Quasar Science Resources S.L for European Space Agency (ESA), ESAC, Camino Bajo del Castillo s/n, 28692 Villanueva de la Cañada, Madrid, Spain

⁹CRESST and X-ray Astrophysics Laboratory, NASA Goddard Space Flight Center, Greenbelt, MD 20771, USA

¹⁰Department of Physics and Astronomy, University of Southampton, Highfield, Southampton SO17 1BJ, UK

¹¹Department of Physics and Astronomy, FI-20014 University of Turku, Finland

¹²Space Research Institute of the Russian Academy of Sciences, Profsoyuznaya Str. 84/32, Moscow 117997, Russia

¹³Nordita, KTH Royal Institute of Technology and Stockholm University, Roslagstullsbacken 23, SE-10691 Stockholm, Sweden

¹⁴Space Sciences Laboratory, University of California, 7 Gauss Way, Berkeley, CA 94720-7450, USA

¹⁵Institute of Astronomy, Madingley Road, Cambridge, CB3 0HA, UK

¹⁷Remeis-Observatory and Erlangen Centre for Astroparticle Physics, Friedrich-Alexander-Universität Erlangen-Nürnberg, Sternwartstr. 7, 96049 Bamberg

¹⁶Centre for Astrophysics Research, University of Hertfordshire, College Lane, Hatfield AL10 9AB, UK

*To whom correspondence should be addressed; E-mail: matteo.bachetti@inaf.it.

M82 X-2 is the first pulsating ultraluminous X-ray source (PULX) discovered. The luminosity of these extreme pulsars, if isotropic, implies an extreme mass transfer rate. An alternative is to assume a much lower mass transfer rate, but an apparent luminosity boosted by geometrical beaming. Only an independent measurement of the mass transfer can help discriminate between these two scenarios. In this Paper, we follow the orbit of the neutron star for seven years, measure the decay of the orbit, and demonstrate that this orbital decay is driven by extreme mass transfer of more than 150 times the mass transfer limit set by the Eddington luminosity. This measurement shows that the mass available to the accretor is more than enough to justify its luminosity, with no need for beaming. This also strongly favors models where the accretor is a highly-magnetized neutron star.

One-sentence summary: We measure the decay of the orbit of the ultraluminous pulsar M82 X-2, providing evidence of extreme mass transfer and, as a consequence, a high neutron star magnetic field.

Introduction The luminosity of accreting sources is largely driven by the amount of matter that is transferred onto the accreting object, whether it be from a donor star for typical neutron stars and stellar mass black holes, or an accretion disk for supermassive black holes at the centers of galaxies (*I*). There is a classical limit to the mass transfer, which corresponds to the mass accretion rate that leads to a balance between the force of radiation pressure pushing outward and the gravitational force acting inward on an accreting object of mass M . For spherical hydrogen accretion, this corresponds to the Eddington luminosity:

$$L_{\text{Edd}} \approx 1.3 \cdot 10^{38} \frac{M}{M_{\odot}} \text{ erg s}^{-1} \quad (1)$$

Therefore, the extreme luminosity of ultraluminous X-ray sources (ULXs) (2, 3) led many to think that these sources were powered by intermediate-mass black holes. Over the years, multiple pieces of evidence cast doubt on the applicability of this classical limit on ULXs (4–6). Eventually, the discovery of pulsating ultraluminous X-ray sources (PULXs; (7), hereafter B14), accreting neutron stars radiating hundreds of times above their Eddington limits, demonstrated that super-Eddington accretion was a viable explanation for the majority of ULXs. It is still unclear how these pulsars (pulsating neutron stars) emit this extreme luminosity. Some argue that the isotropic luminosity is much lower, and the observed luminosity is boosted by geometrical beaming, driven by the collimation of a (less extreme) super-Eddington disk (8). This interpretation has found some support in global MHD simulations of accreting black holes and neutron stars, where mild to extreme geometrical beaming is observed (e.g. (9, 10)). However, these simulations assume a very small magnetic field of the neutron star, if any, and this collimation effect is likely to be lessened when the magnetic field of the pulsar is strong. In fact, other models explain the luminosity with arguments centered on the magnetic field of the pulsar, like the reduction of the Thomson scattering cross section in high magnetic fields (11) and/or the effect of multipolar components of the field (12). It is also possible that the solution is a mixture of genuine super-Eddington accretion and a small amount of beaming (13).

A key difference between these models is the relation that they assume between the mass accretion rate and the luminosity, linear in the low-beaming scenario, almost quadratic ($L \propto (1 + \log \dot{m})\dot{m}^2$) in the other, due to the quadratic dependence of beaming on the mass accretion rate (14). In other words, beaming models infer a much lower mass transfer rate between the donor star and the neutron star.

An independent measurement of the mass transfer is key for disentangling these two scenarios. One way to measure this transfer of matter between two orbiting objects is through the observation of changes in the orbital parameters, such as the orbital period and semi-major

axis (15).

Orbital decay To describe a change of the orbital period over time, it is customary to measure the time that a star reaches an important phase of the orbit, and compare it with the expected time given the previous orbital solution. For circular orbits with no eclipses, it is common to use one of the two intersections between the orbit and the plane perpendicular to the line of sight passing through the center of mass of the binary system. These points of the orbit are called nodes; the *ascending node* is the node that the pulsar crosses when moving away from the observer. The expected time of passage at the ascending node after n orbits $T_{\text{asc},n}$ (for simplicity, we drop the *asc* when n or other indices are present), in the presence of an orbital derivative, can be expressed as (cfr. (16, 17)):

$$T_n = T_0 + n P_{\text{orb}} + \frac{1}{2} n^2 P_{\text{orb}} \dot{P}_{\text{orb}} + \frac{1}{6} n^3 P_{\text{orb}}^2 \ddot{P}_{\text{orb}}^3 + \dots \quad (2)$$

By using a previously determined ephemeris as a baseline, we can measure the delay of the measured T_{asc} from the expected one. When plotting this delay, offsets indicate an uncertainty in T_{asc} , linear trends an uncertainty of P_{orb} , and parabolic trends an orbital period derivative:

$$\delta T_n(t) = \delta T_0 + \frac{t - t_0}{P_{\text{orb}}} \delta P_{\text{orb}} + \frac{1}{2} \frac{\dot{P}_{\text{orb}}}{P_{\text{orb}}} (t - t_0)^2, \quad (3)$$

where we substituted $n = (t - t_0)/P_{\text{orb}}$. In 2020-2021, we observed the M82 field with *NuSTAR* (18) 11 times (five pairs of two observations plus a single one), and we found significant pulsations in four of them. The search was conducted using the Rayleigh test (19) over three parameters: spin frequency, frequency derivative, and orbital phase. By reanalyzing all *NuSTAR* observations of the M82 field, running an additional search using only hard photons (8–30 keV), and also allowing for a negative spin derivative, we detected the pulsar in two more observations in 2014 and 2016. See the Material and Methods section for more details.

Through pulsar timing, we tracked the orbital phase of M82 X-2 over seven years from 2014 to 2021 (Figure 1; see Methods for details of the fitting procedure used). This allowed us to detect a clear parabolic trend in these phases, and allowed us to measure

$$\frac{\dot{P}_{\text{orb}}}{P_{\text{orb}}} \approx -7.7(1.4) \cdot 10^{-6} \text{ yr}^{-1}, \quad (4)$$

which means that the 2.5-day orbital period of M82 X-2 is decreasing by $\dot{P}_{\text{orb}} \sim -5 \cdot 10^{-8} \text{ s s}^{-1}$ (see Figure 1 and Table 1).

The observed orbital decay is compatible with the mass transfer from a more massive donor star to a neutron star (15), see Methods). Assuming a pulsar mass $M_p = 1.4M_\odot$ and a donor mass $M_d = 8M_\odot$ (which corresponds to the mean of the probability distributions of masses, see Methods), it is straightforward to estimate the mass transfer rate from the observed orbital decay, assuming conservative mass transfer, as $\dot{M}_d \approx -4.4 \cdot 10^{-6} M_\odot \text{ yr}^{-1}$. This corresponds to ~ 185 times the Eddington limit, assuming an Eddington mass accretion rate corresponding to $\dot{M}_{\text{Edd}} \approx 1.5 \cdot 10^{18} \text{ g s}^{-1} \approx 2.4 \cdot 10^{-8} M_\odot \text{ yr}^{-1}$. This is the mass that the donor transfers into the Roche lobe of the neutron star. It is possible that part of this matter leaves the system through fast winds launched from the super-Eddington disk (20, 21). However, this mass loss from the vicinity of the accretor produces only a small correction to the conservative case. Isotropic mass loss from the donor, instead, as one would expect from stellar winds, would *compensate* for this effect, expanding the orbit. Therefore, the estimate above is a *lower limit* to the mass transfer. This mass exchange exceeds both that inferred from the apparent bolometric luminosity of the source (which is at most ~ 100 times the Eddington limit, see B14), or the one inferred from beaming scenarios (36 times Eddington, (8)). See Figure 2 for details.

How much matter is really accreting? It is expected that a fraction of this transferred mass will abandon the system in the form of fast winds (14, 22). Evidence of these winds has indeed

been observed, both from direct signatures of relativistic outflows (20) and from the observation of nebulae around ULXs (23). According to the classical scenario, the disk remains thin until matter reaches the spherization radius R_{sph} , where strong disk winds carry away excess matter and maintain a local Eddington limit (see Figure 3). In the black hole case, neglecting the advection of heat, this goes down to the compact object itself, and the accretion onto the compact object is actually close to the Eddington limit even if the mass transfer rate from the donor is much higher (22). Accounting for advection limits the locally radiated flux, and in turn the removal of mass in outflows, producing a mass accretion rate on the compact object which is at most a factor ~ 2 lower than the mass transfer rate from the donor (4). In neutron stars we can expect that once the disk reaches the inner radius R_{in} , the interaction with the magnetic field and the effect of advection of heat lead to an optically thick curtain and the suppression of winds (24). According to this scenario, the winds outside R_{in} cannot expel more than $\sim 60\%$ of the matter, and maintain a large opening angle even at the highest accretion rates (25). Below, we follow this approach and assume that the mass loss from disk winds only happens outside R_{in} .

Spin equilibrium, and a large magnetic field Thanks to the new detections listed above, we found that for at least part of the time between 2016 and 2020 the pulsar continued to spin down (slow down its rotation) as reported by B20, because the frequency (~ 0.721 Hz) observed in 2020 was lower than observed in 2016 (~ 0.723 Hz). However, since then, the neutron star appears to be alternating phases of spin up and spin down around ~ 0.721 Hz. In at least one observation in 2016 and probably in another in 2021, the pulsar was spinning down while accreting (see Figure 4 and Table S1). In summary, the spin evolution of M82 X-2 strongly points to a situation of *spin equilibrium* (see Figure 3 and Supplementary Text), a regime where the outward pressure from the rotating magnetic field balances almost exactly the ram pressure

from the infalling matter. In this condition, spin up and spin down can be produced with small changes of accretion rate (26), and it is possible to confidently estimate the magnetic field of the neutron star, by equating the analytical formulas for the inner radius R_{in} to the corotation radius R_{co} , at which the angular velocity of the matter in the disk equals the one of the star (see Supplementary Text).

Over the years, many models have been proposed to describe the interaction between the plasma in the disk and the magnetic field lines (27–29). Despite large differences in the treatment of the details of this interaction, these models make estimates for the magnetic field in spin equilibrium compatible within \sim one order of magnitude when the inner radius and the mass accretion rate are fixed (30). Until now, different Groups have used the observed luminosity as a proxy for the mass accretion rate, and this produced very different estimates depending on the assumption of the beaming fraction. In addition, different works used different assumptions on the position of the inner radius, with the high-magnetic field models assuming spin equilibrium (31, 32) and the beaming models being incompatible with it (8). Thanks to this work, we can fix these two important variables, leading to an interpretation of M82 X-2 being a highly magnetized neutron star ($B > 10^{13}$ G) with practically any of these models (see Supplementary Text for more details).

In addition, we find a strong disagreement with the often-used beaming estimate of $b \sim 73/\dot{m}^2$ (14). In our case, this would imply $b \sim 0.002$, or an opening angle of $\sim 4^\circ$, and, even assuming that the accretion on the neutron star is Eddington-limited, an apparent luminosity of ~ 500 times Eddington, much higher than observed (see Supplementary Text for additional arguments). Our mass transfer is actually larger than inferred from the isotropic luminosity, meaning that there is sufficient mass to power the observed luminosity and suggesting that genuine super-Eddington emission from the surface of the neutron star is at work. Mechanisms involving large and/or non-dipolar magnetic fields are promising in explaining luminosities

hundreds of times above the Eddington limit (11, 12).

Discussion The measured orbital period derivative can inform the theoretical study of ULX progenitors and their outcomes (33,34). Past works (35–37) have investigated this problem, with predicted donor masses and binary evolution paths that can be compared with our observations.

The low-mass ($< 8M_{\odot}$), slightly evolved donors found by (35) have very high mass transfer rates ($\geq 3 \cdot 10^{-5} M_{\odot} \text{yr}^{-1}$), that can be reconciled with our results only if a strong mass loss from the donor is assumed and/or the mass of the accretor is relatively high. Such a strong mass loss was an ad-hoc component of the simulations from (35), which helped stabilize the mass transfer, but is unexpected from current models of stellar wind unless the donor is very massive or metallicity is very high (38). X-ray heating might in principle enhance wind production, and produce very large mass losses provided that the X-ray source illuminates the donor star and the efficiency of irradiated wind production is high (39).

Similar results come from (37), where the lowest-mass donors are favored and the donor of M82 X-2 is barely included in the stable mass transfer parameter range. On the other hand, the high-mass systems investigated by (36) predict compatible mass transfer rates, but they assume very high-mass stars that have already undergone a part of their evolution (i.e. they do not evolve the system from Zero-age main sequence), and it is unclear if their formation path is compatible with the possible formation paths of ULXs. In particular, the progenitor of the neutron star must have been more massive than the donor at some point, meaning that it would have transferred some mass to the present-day donor. Therefore, a comparison with the current models would seem to imply that M82 X-2 represents a relatively short-lived, high-mass transfer phase of the binary evolution, quickly leading to a common envelope. This seems at odds with the observation of 1 Myear-old optical bubbles around ULXs (23).

The length and the stability of the mass transfer has important implications, for example, for

understanding if neutron star ULXs can collapse into black holes, and if their binary systems can be the progenitors of double-compact object binaries and/or future GW sources (e.g. (40, 41)). We encourage further studies of ULX populations and progenitors incorporating the new evidence reported in this Paper.

Recently, various authors have investigated accreting objects as sources of fast radio bursts (FRB; e.g. (42)). In the models predicting that the FRB is produced in regions far away from the compact object originating the emission, a shock needs to be created in a dense, magnetized medium. In particular, (43) suggest that super-Eddington accretion might be a fundamental ingredient in these models to account for FRB luminosities and timescales, also in relation to the observed periodicities observed in some of them (44). This would make ULXs with a precessing inner disk a likely progenitor of repeating FRBs, but in order to work, it would require a very small beaming fraction.

In this framework, our work seems to provide evidence that systems like M82 X-2 are not favoured as periodic FRB progenitors.

References

1. J. Frank, A. King, D. J. Raine, *Accretion Power in Astrophysics: Third Edition* (Accretion Power in Astrophysics, 2002).
2. P. Kaaret, H. Feng, T. P. Roberts, *Annual Review of Astronomy and Astrophysics* **55**, 303 (2017).
3. S. N. Fabrika, K. E. Atapin, A. S. Vinokurov, O. N. Sholukhova, *Astrophys. Bull.* **76**, 6 (2021).
4. J. Poutanen, G. Lipunova, S. Fabrika, A. G. Butkevich, P. Abolmasov, *MNRAS* **377**, 1187 (2007).

5. J. C. Gladstone, T. P. Roberts, C. Done, *MNRAS* **397**, 1836 (2009).
6. M. Bachetti, *et al.*, *ApJ* **778**, 163 (2013).
7. M. Bachetti, *et al.*, *Nat.* **514**, 202 (2014).
8. A. King, J.-P. Lasota, W. Kluźniak, *MNRAS Let.* **468**, L59 (2017).
9. Y.-F. Jiang, J. M. Stone, S. W. Davis, *The Astrophysical Journal* **796**, 106 (2014).
10. D. Abarca, K. Parfrey, W. Kluźniak, *The Astrophysical Journal* **917**, L31 (2021).
11. A. A. Mushtukov, V. F. Suleimanov, S. S. Tsygankov, J. Poutanen, *MNRAS* **454**, 2539 (2015).
12. N. Brice, S. Zane, R. Turolla, K. Wu, *Monthly Notices of the Royal Astronomical Society* **504**, 701 (2021).
13. G. L. Israel, *et al.*, *Science* **355**, 817 (2017).
14. A. R. King, *MNRAS Let.* **385**, L113 (2008).
15. T. M. Tauris, E. P. J. van den Heuvel, *Compact stellar X-ray sources* pp. 623–665 (2006).
16. R. Kelley, S. Rappaport, R. Petre, *The Astrophysical Journal* **238**, 699 (1980).
17. M. Falanga, *et al.*, *Astronomy and Astrophysics* **577**, A130 (2015).
18. F. A. Harrison, *et al.*, *ApJ* **770**, 103 (2013).
19. K. V. Mardia, *Journal of the Royal Statistical Society: Series B (Methodological)* **37**, 349 (1975).
20. C. Pinto, A. Fabian, M. Middleton, D. Walton, *arXiv* p. arXiv:1611.00623 (2016).

21. P. Kosec, *et al.*, *Monthly Notices of the Royal Astronomical Society* **479**, 3978 (2018).
22. N. I. Shakura, R. A. Sunyaev, *A&A* **24**, 337 (1973).
23. M. W. Pakull, L. Mirioni, *arXiv* p. 0202488 (2002).
24. A. A. Mushtukov, V. F. Suleimanov, S. S. Tsygankov, A. Ingram, *Monthly Notices of the Royal Astronomical Society* **467**, 1202 (2017).
25. A. A. Mushtukov, A. Ingram, M. Middleton, D. I. Nagirner, M. van der Klis, *Monthly Notices of the Royal Astronomical Society* **484**, 687 (2019).
26. C. R. D'Angelo, H. C. Spruit, *Monthly Notices of the Royal Astronomical Society* **420**, 416 (2012).
27. P. Ghosh, F. K. Lamb, *ApJ* **223**, L83 (1978).
28. Y.-M. Wang, *The Astrophysical Journal* **465**, L111 (1996).
29. A. Chashkina, P. Abolmasov, J. Poutanen, *Monthly Notices of the Royal Astronomical Society* **470**, 2799 (2017).
30. X. Chen, W. Wang, H. Tong, *Journal of High Energy Astrophysics* **31**, 1 (2021).
31. S. S. Tsygankov, A. A. Mushtukov, V. F. Suleimanov, J. Poutanen, *MNRAS* **457**, 1101 (2016).
32. S. Dall'Osso, R. Perna, L. Stella, *MNRAS* **449**, 2144 (2015).
33. K. Pavlovskii, N. Ivanova, K. Belczynski, K. X. Van, *Monthly Notices of the Royal Astronomical Society* **465**, 2092 (2017).
34. W. Kluźniak, J.-P. Lasota, *MNRAS Let.* **448**, L43 (2015).

35. T. Fragos, T. Linden, V. Kalogera, P. Sklias, *The Astrophysical Journal* **802**, L5 (2015).
36. M. Quast, N. Langer, T. M. Tauris, *Astronomy and Astrophysics* **628**, A19 (2019).
37. D. Misra, T. Fragos, T. M. Tauris, E. Zapartas, D. R. Aguilera-Dena, *Astronomy and Astrophysics* **642**, A174 (2020).
38. J. S. Vink, *New Astronomy Reviews* **52**, 419 (2008).
39. X.-Q. Han, L. Jiang, W.-C. Chen, *The Astrophysical Journal* **914**, 109 (2021).
40. P. Marchant, *et al.*, *Astronomy and Astrophysics* **604**, A55 (2017).
41. I. Mandel, F. S. Broekgaarden, Rates of Compact Object Coalescences (2021).
42. E. Waxman, *ApJ* **842**, 34 (2017).
43. N. Sridhar, *et al.*, *ApJ* **917**, 13 (2021).
44. Chime/Frb Collaboration, *et al.*, *Nature* **582**, 351 (2020).
45. D. J. Walton, *et al.*, *The Astrophysical Journal* **826**, 87 (2016).
46. M. Bachetti, *et al.*, *ApJ* **908**, 184 (2021).
47. R. Bucccheri, *et al.*, *A&A* **128**, 245 (1983).
48. M. Bachetti, *et al.*, *ApJ* **891**, 44 (2020).
49. M. Bachetti, *et al.*, *ApJ* **909**, 33 (2021).
50. K. T. S. Brazier, *Monthly Notices of the Royal Astronomical Society* **268**, 709 (1994).
51. D. A. Leahy, *et al.*, *ApJ* **266**, 160 (1983).

52. B. A. Vaughan, *et al.*, *ApJ* **435**, 362 (1994).
53. M. Bachetti, *Astrophysics Source Code Library* p. ascl:1805.019 (2018).
54. J. Luo, *et al.*, *The Astrophysical Journal* **911**, 45 (2021).
55. Astropy Collaboration, *et al.*, *The Astronomical Journal* **156**, 123 (2018).
56. P. Virtanen, *et al.*, *Nature Methods* **17**, 261 (2020).
57. C. R. Harris, *et al.*, *Nature* **585**, 357 (2020).
58. S. K. Lam, A. Pitrou, S. Seibert, *Proceedings of the Second Workshop on the LLVM Compiler Infrastructure in HPC*, LLVM '15 (Association for Computing Machinery, New York, NY, USA, 2015).
59. J. D. Hunter, *Computing in Science & Engineering* **9**, 90 (2007).
60. D. Foreman-Mackey, D. W. Hogg, D. Lang, J. Goodman, *PASP* **125**, 306 (2013).
61. D. Foreman-Mackey, *The Journal of Open Source Software* **1**, 24 (2016).
62. M. Heida, *et al.*, *The Astrophysical Journal* **871**, 231 (2019).
63. A. King, J.-P. Lasota, *Monthly Notices of the Royal Astronomical Society* **494**, 3611 (2020).
64. I. E. Mellah, J. O. Sundqvist, R. Keppens, *A&A* **622**, L3 (2019).
65. K. A. Stoyanov, R. K. Zamanov, *Astronomische Nachrichten* **330**, 727 (2009).
66. T. M. Tauris, G. J. Savonije, *Spin-Orbit Coupling in X-Ray Binaries*, vol. 567 (eprint: arXiv:astro-ph/0001014, 2001).
67. E. P. J. van den Heuvel, *Interacting Binaries: Topics in Close Binary Evolution*. (1994).

68. G. E. Soberman, E. S. Phinney, E. P. J. van den Heuvel, *Astronomy and Astrophysics*, v.327, p.620-635 **327**, 620 (1997).
69. P. C. Joss, S. A. Rappaport, *Annual Review of Astronomy and Astrophysics* **22**, 537 (1984).
70. S. Fabrika, S. Karpov, P. Abolmasov, O. Sholukhova, G. Fabbiano, *IAU* **230**, 278 (2006).
71. A. M. Cherepashchuk, A. A. Belinski, A. V. Dodin, K. A. Postnov, *Monthly Notices of the Royal Astronomical Society* **507**, L19 (2021).
72. A. Chashkina, G. Lipunova, P. Abolmasov, J. Poutanen, *Astronomy and Astrophysics* **626**, A18 (2019).
73. A. D. Sutton, T. P. Roberts, M. J. Middleton, *MNRAS* **435**, 1758 (2013).
74. A. Gúrpide, O. Godet, G. Vasilopoulos, N. A. Webb, J. F. Olive, Discovery of a recurrent spectral evolutionary cycle in the ultraluminous X-ray sources Holmberg II X-1 and NGC 5204 X-1 with evidence for periodic flux modulations (2021).
75. M. Brightman, *et al.*, *The Astrophysical Journal* **873**, 115 (2019).
76. P. P. Eggleton, *ApJ* **268**, 368 (1983).
77. L. P. Surkova, M. A. Svechnikov, *VizieR Online Data Catalog* (2004).

Acknowledgments

The authors wish to thank Włodek Kluźniak and Alessandro Ridolfi for useful discussions, and the staff at the NuSTAR Science Operations Center at Caltech for the help in scheduling the observations and the frequent clock correction file updates, that allowed a prompt analysis of the data. MB was funded in part by PRIN TEC INAF 2019 “SpecTemPolar! – Timing analysis

in the era of high-throughput photon detectors”. MH is supported by an ESO fellowship. GLI acknowledges funding from the Italian MIUR PRIN grant 2017LJ39LM. ADJ was funded in part by the Chandra grant 803-0000-716015-404H00-6100-2723-4210-40716015HH83121. JP was supported by the grant 14.W03.31.0021 of the Ministry of Science and Higher Education of the Russian Federation and the Academy of Finland grant 333112. DJW acknowledges support from STFC in the form of an Ernest Rutherford Fellowship. HPE acknowledges support under NASA Contract No. NNG08FD60C.

All the analysis of this Paper was done using open-source software: Astropy, Stingray, HENDRICS, PINT, emcee, corner, scinum, and can easily be verified using the solution in Table 1. Figures were produced using the Matplotlib library and the Veusz software. The data used for this work come from the *NuSTAR* mission and are usually held private for one year, and made public on the High Energy Astrophysics Science archive (HEASARC) afterwards. *NuSTAR* is a Small Explorer mission led by Caltech and managed by JPL for NASA’s Science Mission Directorate in Washington. *NuSTAR* was developed in partnership with the Danish Technical University and the Italian Space Agency (ASI). The spacecraft was built by Orbital Sciences Corp., Dulles, Virginia.

Figures and tables

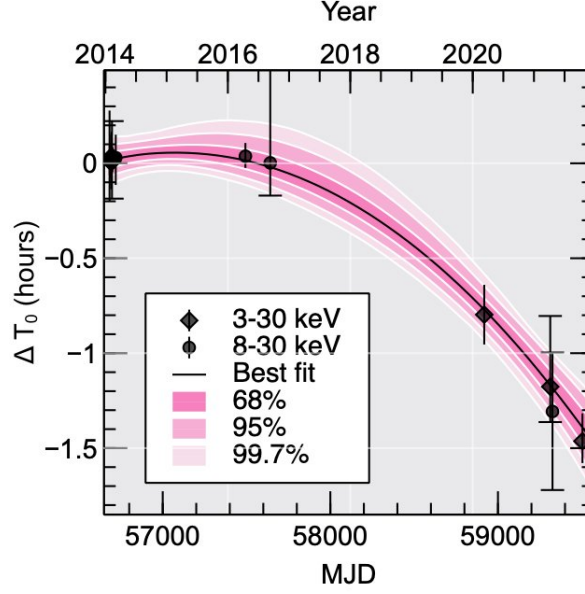


Figure 1: Orbital decay in M82 X-2, measured through the delay of the T_{asc} parameter (time of passage through the ascending node) from Equation 3. For every observation, we selected the energy range that yielded the best constraint. Error bars without caps indicate $1\text{-}\sigma$ uncertainties. Those with caps indicate strict limits (values compatible with a spin derivative $|\dot{f}| < 2 \cdot 10^{-10} \text{ Hz s}^{-1}$). The shaded region indicates the credible intervals on the allowed quadratic solutions, coming from MCMC sampling (described in the Methods and Materials section).

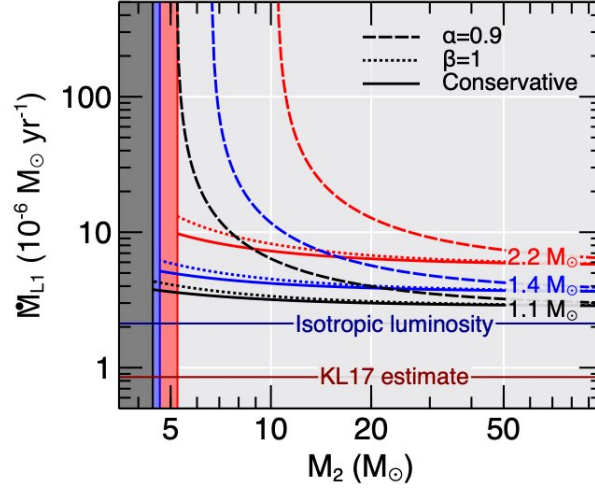


Figure 2: Mass transfer rate towards the accretor (through L1), versus donor mass, given the measured orbital period decay. We estimate the mass transfer rate for different mechanisms of mass loss and different accretor masses. Solid lines indicate conservative mass transfer, dashed lines indicate 90% isotropic mass loss from the donor, and dotted lines indicate 100% mass loss from the proximity of the accretor. The latter is only a small correction to the conservative case, while mass loss from the donor implies a much larger mass transfer rate in order to produce the observed orbital decay. Vertical bands on the left show the limit donor masses given the absence of eclipses, for different accretor masses (same color coding).

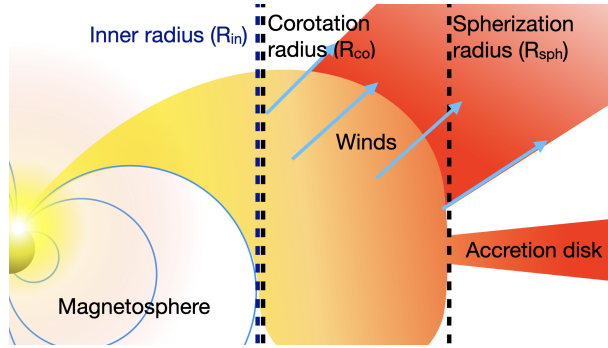


Figure 3: Possible geometry of the accretion region of M82 X-2. The inner radius is close to the co-rotation radius, where the orbital and the neutron star's angular velocities match. In this situation, the star alternates spin up and spin down depending on small changes of the mass accretion rate. Between the spherization radius and the inner radius fast winds are launched, producing mass loss from the system

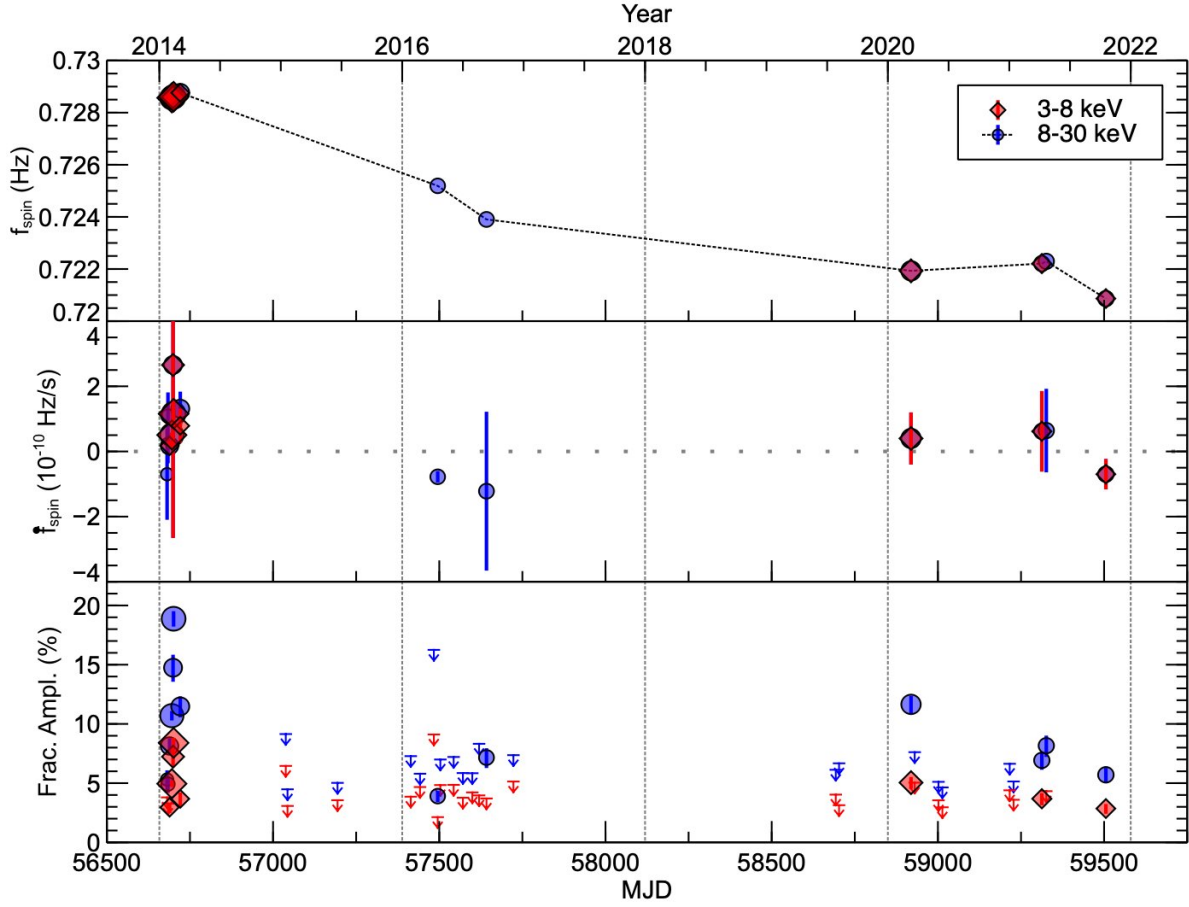


Figure 4: Spin history of M82 X-2 since 2014. Error bars indicate $1\text{-}\sigma$ uncertainties. Different colors indicate different energy bands, confirming that the fractional amplitude of the pulsation is systematically higher above 8 keV. The fractional amplitude measurements are reduced by the presence of M82 X-1, which is spatially unresolved by *NuSTAR*: most non-detections are likely to be driven by the brightness of M82 X-1.

Parameter	Unit	Value (uncert)
P_{orb}	d	2.532971(13)
\dot{P}_{orb}	s s ⁻¹	$-5.4(1.0) \cdot 10^{-8}$
$\dot{P}_{\text{orb}}/P_{\text{orb}}$	yr ⁻¹	$-7.7^{+1.3}_{-1.4} \cdot 10^{-6}$
$a \sin i$	l-sec	22.215(5) (B20)
T_0	MJD	56682.0669(18)

Table 1: Updated orbital parameters for M82 X-2, as determined in this work.

Supplementary materials

Materials and Methods

Supplementary Text

Figs. S1 to S4

Table S1

Materials and Methods

Data reduction

We downloaded all the *NuSTAR* data from the High Energy Astrophysics Science Archive Research Center (HEASARC). We ran `nupipeline` with standard options to produce cleaned event files. This tool produces different event files corresponding to different observing modes: SCIENCE (01), OCCULTATION (02), SLEW (03), SAA (04), CALIBRATION (05), and SCIENCE_SC (06). The modes usable for science are 01 and 06. Note, however, that only mode-01 data are recorded in normal instrumental conditions. Mode-06 data correspond to time intervals where only a subset of the camera head units (CHUs) are available, and the astrometry can be off by 1–2' (See (45) for an example of the astrometry issues in this observing mode). For mode-01 data, we used a region of 70'' around the centroid of the X-ray source corresponding to the position of M82 X-1 and M82 X-2, which is spatially unresolved in *NuSTAR*. The centroid was calculated independently for each observation and for each of the two focal plane modules, as a mismatch of $\sim 10''$ can be expected.

We processed mode-06 data with the `nusplitsc` tool, which separates events corresponding to different CHU combinations. For each of these event files, we adjusted the centroid of the source and repeated the selection done for mode-01 data. Finally, we merged the source-selected event lists from mode-01 and mode-06 data. In only a few cases, due to the source falling on a chip gap, we saw that the light curve showed visible “steps” between intervals corresponding to different CHU combinations. We later verified that the addition or elimination of the problematic intervals did not alter significantly the power around the pulsation frequency ~ 0.7 Hz.

Finally, we ran `barycorr` to refer the photon arrival times to the solar system barycenter. We selected the ICRS reference frame, the DE421 JPL ephemeris, and the position of M82 X-2

determined by *Chandra*. For all observations, we used the latest clock correction file available, that provides an absolute time precision of $\sim 60 \mu\text{s}$. For 30702012002, the observation was too close to the submission of the paper to get a precise clock correction file, which typically needs ~ 1 month of ground station measurements to reach the requested precision (46). We will update the analysis as soon as the new clock correction file is available.

Timing analysis

We largely followed the search strategies used in B20, running Z_1^2 searches (47), also known as the Rayleigh test, on the event arrival times corrected for orbital motion, varying the ascending node passage epoch T_0 on a fine grid between $-P_{\text{orb}}/5$ and $P_{\text{orb}}/5$. This time, the search allowed a range of spin derivatives *for each trial ascending node passage value*. For the search in the $f - \dot{f}$ plane, we used the “quasi-fast folding algorithm” (48), that calculates the Z_1^2 on pre-binned profiles (49), using at least 16 bins for the folded profiles. Moreover, we ran the search both in the full energy band and between 8 and 30 keV. As we show below, this allowed six new detections, four in new observations and two in archival observations. For each detection, we then ran the search again around the best solution, using the slow (non-binned) algorithm this time, to evaluate proper confidence limits on the parameters.

This multi-dimensional search poses questions on how to evaluate the error bars and/or confidence limits on the spin and orbital parameters. The spin parameters vary so rapidly that they are only loosely constrained when observations are not more than a \sim week apart. There is no way to reliably phase connect separate observations. The number of trials considered in the frequency domain are the standard independent numbers of trials, corresponding to the FFT resolution of $1/T$, where T is the observation length. If the signal is not detected with a simple search over frequency with the orbital parameters previously determined from other observations, we multiply by the independent number of trials over the passage through the ascending

node that are needed until a promising signal is found. At this point, the signal is always detected without a frequency derivative, and further refinements do not increase the number of trials, but they are evaluated using standard statistical tests. As previously noted by (50) and used by (13), the Rayleigh test is a very good approximation of the (negative) log likelihood of a sinusoidal signal in the null hypothesis of no signal, and one can in principle apply the Akaike Information Criterion or other likelihood comparison tests to choose whether an additional parameter (e.g. the frequency derivative) improves the detection significantly. However, when comparing the results using multiple parameters or calculating confidence intervals, the null hypothesis is no longer the absence of signal, but rather that there is a signal with a given power. Therefore, we use an approach similar to (50) to evaluate the confidence intervals, starting from the following formula for the probability to detect a signal with the Rayleigh test. Given a signal:

$$y = \lambda(1 + a \sin \omega t), \quad (5)$$

the expected power in a periodogram in Leahy (51) normalization or in the Z_1^2 search calculated from N photons is

$$P_s = N \frac{a^2}{2}. \quad (6)$$

The probability to measure a given power P is then given by the noncentral chi-squared distribution with two degrees of freedom (χ_2^2):

$$p(P|P_s) = e^{-(P+P_s)/2} I_0 \left(\sqrt{PP_s} \right) \quad (7)$$

where I_0 is the modified first-order Bessel function of order 0. This distribution is efficiently implemented in `scipy`.

We emphasize that we are measuring P and inferring confidence intervals of P_s , so we are interested in $p(P_s|P)$, not $p(P|P_s)$. We use minimization to find the P_s that produces the observed P as a given quantile, and define the corresponding confidence limit on the parameters as the parameter space yielding $P \geq P_s$.

A similar procedure can be applied for upper limits (52). Say we observe $P = 40$ and, given the number of independent frequency values in the search, this is not considered a detection. We calculate an upper limit on pulsations as follows: first, we ask ourselves what is the P_s that can produce $P = 40$ to a confidence c . Since noise powers act in the complex plane and can partially cancel signal power, and we want an *upper* limit, this estimated P_s will be *larger* than P . Next, we transform this P_s into a modulation amplitude by inverting Equation 6.

Our timing analysis was implemented using the open source packages `HENDRICS` (53), `stingrayhuppenkothenStingraySpectraltimingSoftware2016`, `pint` (54), all of which are based on `astropy` (55), `scipy` (56), and `numpy` (57). For better performance, we used the libraries `numba` (58) Plots were produced using `Veusz`¹ and `Matplotlib` (59). The upper limit calculation presented here was implemented in `stingray`.

Constraints on spin and orbital parameters

NuSTAR made three pairs of observations of M82 X-2 during AO-5, and two pairs of observations during AO-6 (PI Bachetti).

We ran a search for pulsations as soon as each observation was carried out, using the techniques described above. We allowed three free parameters in the search: T_{asc} , f_{spin} , and \dot{f}_{spin} . The new observations cannot constrain the projected semi-major axis $a \sin i$ better than the 2014 observations, and this parameter is highly correlated with the others if the observation duration is shorter than the orbital period. Given that the effects we are testing are orders of magnitude below the error bar on this parameter, we fix it to the solution by B20. This said, note that the spin derivative was not a free parameter in the pulsation searches done by B20. Also, we searched using two ranges of energy: 3–30 keV and 8–30 keV, as M82 X-2 pulsations are known to be sometimes better detectable above 8 keV. We summarize the results in Table S1. Among

¹<https://veusz.github.io/>

the six total observations during AO-5, we could detect pulsations only in one. Of the four observations in AO-6, we detected pulsations in two. All these observations showed a significant delay in T_{asc} using the solution in B20. The detection from AO-5 is very significant and allows to constrain the orbital phase despite a lever arm of only 1/3 of the orbit (See Figure S1). The detections from AO-6 are less significant and the T_{asc} is highly correlated with \dot{f}_{spin} . We tried to join the two observations in each pair and run the 3-D search above. However, it is clear that the spin up is not described by a single frequency derivative, and a search over larger parameter spaces produced weak constraints. Nevertheless, by putting a hard limit on the allowed values of $|\dot{f}_{\text{spin}}| < 2 \cdot 10^{-10} \text{ Hz s}^{-1}$, motivated by being well above the maximum previously observed spin up/down of M82 X-2, we obtained a strong constraint on the orbital phase, as discussed below.

We also re-ran a pulsation search using all available observations, and we found significant ($\geq 5\sigma$) pulsations in two archival datasets, corresponding to ObsIDs 30101045002 and 80002092002. In both observations, pulsations are more strongly detected in the 8–30 keV energy band. Moreover, surprisingly, we find that during 30101045002 the pulsar was instantaneously spinning *down*. This is the first time that M82 X-2 is found spinning down while accreting and pulsating, and provides clear evidence that a significant part of the torque from the disk is happening outside the corotation radius. This is probably why B20 only obtained marginal evidence for pulsations in this ObsID. This new detection is important because pulsations are detected over a ~ 4 -day interval, which is long enough to provide an excellent constraint on T_0 .

Orbital fitting

Using the new T_{asc} values, we infer the orbital decay of M82 X-2 using a Bayesian model. First, we separate observations where the 3D search hit the boundary set by the maximum

spin derivative of $2 \cdot 10^{-10} \text{ Hz s}^{-1}$ from those that have well-constrained spin derivatives. For the latter, we assume Gaussian uncertainties; these form our data set for parameter inference. The observations where inferring the spin derivative was not possible (hereafter the *bracketed* points, shown with capped error bars in Figure 1) nevertheless place important constraints on the orbital evolution. These constraints are effectively implemented as a flat prior on ΔT_0 at the time of these observations, forcing the maximum absolute spin derivative to remain below $2 \cdot 10^{-10} \text{ Hz s}^{-1}$.

The following equation serves as the orbital evolution model:

$$\Delta T_0 = a + \frac{b}{P_{\text{orb}}}(t - T_0) + 0.5 \cdot 10^{-6} c \frac{86400}{365}(t - T_0)^2 \quad (8)$$

where t , T_0 and P_{orb} are expressed in days, ΔT_0 is the delay of T_{asc} in seconds, a is a correction to T_0 in seconds, b is a correction to P_{orb} in seconds and c is the new value of $\dot{P}_{\text{orb}}/P_{\text{orb}}$ in units of 10^{-6} yr^{-1} . The baseline solution from B20 was $T_{0,\text{B20}} = \text{MJD } 56682.0661$, $P_{\text{orb},\text{B20}} = 2.532948 \text{ d}$, and $\dot{P}_{\text{orb}} = 0 \text{ s s}^{-1}$. Priors for a , b and c were uniform and noninformative; in checks, we found that the width of the prior has no significant effect on our posterior inference. Additional prior information comes from the constraints on ΔT_0 coming from the bracketed points, which are implemented as a validation function: any model that produces values outside of the allowed prior range of the bracketed points are deemed impossible, and the associated parameters assigned a prior probability of zero.

We first perform a Maximum-A-Posteriori fit with a standard Gaussian likelihood. The solution serves as an initialization of a Markov Chain Monte Carlo (MCMC) sampler as implemented in the `emcee` (60) library. Using 32 walkers, we ran the chains for 100,000 steps. We calculated the autocorrelation “time”, which was at most 46 steps. We thinned the chain by a factor 23 (half the autocorrelation length) and discarded 920 steps (20 times the autocorrelation length) as burn-in. The resulting marginal posterior probability distributions are plotted

using the `corner` library (61) in Figure S2. We find posterior means and credible intervals of $a = 72 \pm 160$, $b = 1.8^{+1.1}_{-1.0}$, and $c = -7.7^{+1.3}_{-1.4}$. Using these values, we corrected the orbital parameters as $T_0 = T_{0,\text{B20}} + a \text{ sec}$, $P_{\text{orb}} = P_{\text{orb,B20}} + b \text{ sec}$, $\dot{P}_{\text{orb}} = c \cdot 10^{-6} M_{\odot} \text{ yr}^{-1}$ to obtain the values in Table 1.

Supplementary Text

Important radii

Around an accreting neutron star, we can define two important radii: the first, the *corotation radius* R_{co} , is the radius at which the Keplerian angular velocity in the disk equals the angular velocity of the neutron star:

$$R_{\text{co}} = \left(\frac{GM p_{\text{spin}}^2}{4\pi^2} \right)^{\frac{1}{3}}. \quad (9)$$

where p_{spin} is the rotation period of the neutron star, M its mass, and G the Universal Gravitational constant.

The second is called the *magnetospheric radius*, or inner radius, or truncation radius. Within this radius, the accretion disk gets disrupted, and matter gets captured by the magnetic field lines and conveyed to the magnetic poles of the neutron star:

$$R_{\text{in}} = \xi \left(\frac{\mu^4}{GM\dot{M}^2} \right)^{\frac{1}{7}} \quad (10)$$

where μ is the magnetic dipole moment, \dot{M} the mass accretion rate, and $\xi \sim 0.5$ encodes a number of effects like the accretion geometry (e.g. disk versus isotropic accretion) and the details of the interaction between the plasma and the different components of the magnetic field.

According to accretion theory, the relative position of R_{co} and R_{in} is what determines whether a neutron star will *spin up* (accelerate its rotation) during accretion or *spin down* (slow down its rotation). The matter captured by the magnetic field of the neutron star at a given

radius is orbiting with a given angular velocity, and will transfer angular momentum to the neutron star through the magnetic field lines. Outside R_{co} , this velocity is lower than the angular velocity of the neutron star, while it is higher inside. Therefore, roughly speaking, if $R_{\text{in}} < R_{\text{co}}$ the star spins up, and if $R_{\text{in}} > R_{\text{co}}$ it spins down. Various corrections can be made, integrating the torque from the matter outside and inside the corotation radius, and different authors come up with different prescriptions that can in general be treated by multiplying R_{in} by a factor of order 1 (27, 28). When $R_{\text{in}} \sim R_{\text{co}}$, small changes of accretion rate move the inner radius back and forth around R_{co} , and we can expect the source to alternatively spin up and down. This situation is called **spin equilibrium**.

When $R_{\text{in}} \gg R_{\text{co}}$, the rotating magnetic field is able to swipe away the in the disk, and it is expected that accretion onto the neutron star will stop. This is known as *propeller* regime.

Around a super-Eddington accreting source, a third important radius is often cited, the *spherization* radius at which the disk departs from an ideal thin disk and part of the mass is ejected in winds (22):

$$R_{\text{sph}} = \frac{27}{4} R_g \frac{\dot{M}}{\dot{M}_{\text{Edd}}} \quad (11)$$

where the Eddington mass accretion rate $\dot{M}_{\text{Edd}} \approx L_{\text{Edd}}/\eta c^2 \approx 1.6 \cdot 10^{18} \text{ g s}^{-1}$ for a $1.4\text{-}M_{\odot}$ neutron star, where $\eta \approx 0.15$ is the efficiency, $R_g = GM/c^2$ is the gravitational radius, and c is the speed of light.

Donor star

The mass function determined through timing gives important insights on the kind of donor star we can expect:

$$f = \frac{M_d^3 \sin^3 i}{(M_p + M_d)^2} = \frac{\Omega_{\text{orb}}^2}{G} (a_p \sin i)^3 \approx 1.83 M_{\odot} \quad (12)$$

where $\Omega_{\text{orb}} = 2\pi/P_{\text{orb}}$ is the orbital angular velocity, $a_p \sin i$ is the projected semi-major axis of the pulsar orbit, M_d is the mass of the donor, M_p is the mass of the pulsar, and i is the

inclination. Note that the Ω_{orb} and $a_p \sin i$ are measured from pulsar timing, while the left-hand side can be used to infer the donor mass given reasonable assumptions about the pulsar mass and the inclination.

Since $\sin i$ cannot be larger than 1 (orbit edge-on), this poses a hard lower limit to the donor star mass, that cannot be less than $3.56 M_\odot$ (assuming a neutron star mass of $1.4 M_\odot$). The absence of eclipses from a (most likely) Roche-Lobe filling donor pushes the lower limit to $\sim 5 M_\odot$ (7) and corresponds to an upper limit on the inclination of $\sim 60^\circ$. An unlikely donor mass of $100 M_\odot$ corresponds instead to an inclination of $\sim 17^\circ$, which we take as a lower limit.

Similar arguments can be used to constrain the donor radius. Assuming Roche Lobe overflow, the size of the donor is fixed by the mass ratio and orbital separation.

With these constraints in mind (see Figure S3), and compared with known populations of donor stars in HMXBs, the most probable candidates are O/B giant stars between $5\text{--}100 M_\odot$. Between $\sim 17^\circ$ ($100 M_\odot$ donor) and $\sim 60^\circ$ ($5 M_\odot$ donor), we assume all orientations to be equally probable. This means that the values of the cosine of the inclination are equally probable between the two limiting cases $\cos 60^\circ$ and $\cos 17^\circ$. This gives an average inclination of $\sim 43^\circ$, corresponding to a donor mass of $\sim 7.8 M_\odot$. Note that an archival search in HST data found several stars of this range of masses which could in principle be the donor (62).

Mass transfer

By differentiating the formula for the orbital angular momentum and Kepler's third Law, it can be shown how the orbital separation and the orbital period change as a response to mass transfer or angular momentum changes (e.g. (15)):

$$\frac{2}{3} \frac{\dot{P}_{\text{orb}}}{P_{\text{orb}}} = \frac{\dot{a}}{a} = 2 \frac{\dot{J}}{J} - 2 \frac{\dot{M}_d}{M_d} - 2 \frac{\dot{M}_p}{M_p} + \frac{\dot{M}_d + \dot{M}_p}{M_d + M_p} \quad (13)$$

where J is the total angular momentum of the system, \dot{M}_p and \dot{M}_d are the change of mass of the pulsar and the donor, a is the orbital separation. \dot{M}_d is negative and \dot{M}_p positive, because

the pulsar is accreting from the donor.

A number of phenomena causing changes in orbital angular momentum are discussed in the literature, such as gravitational wave (GW) emission (important in very compact systems such as some binary neutron stars), spin-orbit coupling (when the Roche-filling star's rotation is not synchronized with the orbit), magnetic braking (studied in low-mass X-ray binaries), and mass loss when the ejected mass has specific angular momentum. Given the large donor mass and orbital distance, we do not expect GW emission or magnetic braking to be significant. Moreover, even though they disagree on the exact mass transfer rate, different authors agree that the system is undergoing a strong mass transfer (24, 63). Such a mass transfer rate is difficult to reconcile with mechanisms other than Roche-Lobe overflow (such as wind accretion or even wind Roche Lobe overflow, (64)), and the synchronization timescales are so small that we can also neglect spin-orbit coupling (65, 66). This leaves us with mass loss as the only likely source of angular momentum drain.

Conservative mass transfer has no angular momentum or mass losses from the system (i.e., $\dot{M}_p = -\dot{M}_d$ and $\dot{J} = 0$). In this case, Equation 13 reduces to:

$$\frac{\dot{P}_{\text{orb}}}{P_{\text{orb}}} = 3 \frac{\dot{M}_d}{M_d} \left(\frac{M_d}{M_p} - 1 \right) \quad (14)$$

It is clear that, for $M_d/M_p > 1$, the system responds to a mass transfer from the donor ($\dot{M}_d < 0$) by decreasing the orbital period, as observed.

The non-conservative mass transfer case (when mass is lost from the system in any form) implies a change of the total angular momentum and can be studied by dividing the angular momentum term into different terms. Following the approach by (15, 67, 68),

$$\frac{\dot{J}}{J} = \frac{\alpha + \beta r^2 + \delta \gamma (1 + r)^2}{1 + r} \frac{\dot{M}_d}{M_d} \quad (15)$$

and

$$\dot{M}_p = -(1 - \alpha - \beta - \delta) \dot{M}_d \quad (16)$$

where $r = M_d/M_p$, α indicates the fraction of matter lost directly from the donor², β the fraction lost from fast winds close to the accretor, and δ the fraction lost in a circumbinary disk of radius $a_r = \gamma^2 a$.

It is interesting to show where the three angular momentum losses lead when they dominate the orbital evolution, by developing Equation 13 with Equation 15 and 16.

For the loss from the donor ($\alpha = 1$):

$$\frac{\dot{P}_{\text{orb}}}{P_{\text{orb}}} = \frac{3}{2} \frac{\dot{M}_d}{M_d} \left(\frac{-r}{1+r} \right) \quad (17)$$

Therefore, an isotropic mass loss from the donor leads to an *expansion* of the orbit.

For the loss from the accretor ($\beta = 1$):

$$\frac{\dot{P}_{\text{orb}}}{P_{\text{orb}}} = \frac{3}{2} \frac{\dot{M}_d}{M_d} \left(\frac{2r^2 - r - 2}{1+r} \right) \quad (18)$$

implying that isotropic mass loss from the accretor (e.g., with disk winds) still leads to a *contraction* of the orbit. This is what is believed to happen at extreme mass transfer rates, where we expect strong radiation-driven winds to be launched inside the spherization radius (22). In the limit $r \gg 1$, this is equivalent to the conservative case.

Finally, for the circumbinary disk ($\delta = 1$), we have

$$\frac{\dot{P}_{\text{orb}}}{P_{\text{orb}}} = \frac{3}{2} \frac{\dot{M}_d}{M_d} \left(\frac{2\gamma(1+r)^2 - 2 - r}{1+r} \right) \quad (19)$$

which, for $\gamma \geq 1$ (disk radius larger than orbital separation) and $r > 1$, also produces a contraction of the orbit.

To summarize, the orbital decay we observe is compatible with the effect of mass transfer between a more massive donor and a neutron star (with or without mass loss from the accretor), or with angular momentum loss through an equatorial circumbinary disk, possibly launched by

²Note that in other papers, e.g. (69), α indicates the specific angular momentum. This can create confusion when comparing the different approaches.

the second Lagrangian point L2 ((15), see also Methods). The second possibility only happens in situations where the donor star inflates well beyond its Roche Lobe, and its onset quickly leads to unstable orbital decay and common envelope (37). SS433, a possible ULX analog in our Galaxy (70), might be undergoing such a process. However, in that case, the accretor is believed to be a stellar-mass black hole and the mass ratio is ~ 1 , and this process leads to the *expansion* of the orbit (71), stabilizing the mass transfer. Due to the observation that matter is indeed accreting onto the neutron star, and that we observe many ULXs in nearby galaxies which suggests that this accretion regime is not too short-lived, our analysis favors conservative (or mildly non-conservative) mass transfer from a intermediate/high mass star, with no high-angular momentum mass loss mechanisms.

Magnetic field estimates

Traditional models, such as those proposed by Ghosh and Lamb (27) or Wang (28), consider a thin disk with negligible radiation effects, and the inner radius is given by Equation 10. Therefore, given a mass accretion rate, the position of the inner radius in this model is a function of the dipolar component of the magnetic field, modulo the order-unity constant ξ . Since the source is close to spin equilibrium, as demonstrated by the spin behavior over time (see Figure 4), the inner radius has to be close to the corotation radius. Therefore, equating the inner radius to the corotation radius, we can get an estimate of the magnetic field, as shown in Figure S4 with the blue band. Here, we take into account mass losses in a wind inside R_{sph} , when relevant, until R_{in} . We use the "classical" mass loss obtained when the effects of advection are neglected (22). In this case, the accretion rate drops linearly with radius, and thus an upper limit on the accretion rate, i.e., an upper limit on the mass loss rate, corresponds to an upper limit on R_{in} and a lower limit to the magnetic field strength. Despite this conservative approach, the estimate on the magnetic field is robustly above 10^{13} Gauss. Most models for sub-Eddington accretion

agree within an order of magnitude for the treatment of spin equilibrium (see, e.g., (30)). However, it is possible that these models which are based on the interaction of a magnetized neutron star with a thin disk, with no radiation pressure either from the disk or from the central object, need to be corrected in the case of super-Eddington disks. Chashkina and collaborators (29, 72) have investigated this issue, finding that, indeed, the disk structure changes significantly when radiation pressure becomes dominant. In particular, they find that ξ is not constant, but depends on local (inside the disk) and external (e.g. from the neutron star) radiation pressure, and the amount of advection in the disk. With the transfer rate > 100 Eddington we find in this Paper, the inner radius becomes almost independent of the mass accretion rate and is described by Eq. 61 from (29):

$$\frac{R_{\text{in}}}{R_g} \approx \left(\frac{73\alpha}{24} \right)^{2/9} \left[\lambda \left(\frac{\mu}{10^{30} \text{G cm}^3} \right)^2 \right]^{2/9} \quad (20)$$

where $\alpha \sim 0.1$ is the viscosity in the disk and $\lambda \sim 4 \cdot 10^{10} (M_p/1.4M_\odot)^{-5}$. Figure S4 shows that, for a reasonable range of the viscosity parameter ³ $0.01 < \alpha_v < 0.3$, the estimate of the magnetic field obtained by equating the inner radius to the corotation radius using Equation 20 is similar to the prediction of traditional models using Equation 10, confirming an estimated magnetic field for M82 X-2 above 10^{13} G, as estimated with the classical model and by other authors in the literature (30, 31).

On collimation and beaming

Provided that our assumptions are correct, meaning that possible super-Eddington outflows happen only between R_{sph} and R_{in} , there is no need to invoke strong beaming to explain the high luminosity of M82 X-2, even if we cannot rule out some degree of collimation. The observed bolometric luminosity is actually *lower* than expected from that accretion rate to the neutron star with standard efficiency, and this might be due to partial occultation of the star from the

³We call this parameter α_v instead of α to avoid confusion with the mass loss parameter α

accretion column or disk winds, as observed in other ULXs (73, 74).

Proponents of the beaming models, assuming a much lower mass transfer rate (\dot{M} 36 times Eddington) than the one we measure, find a beaming factor $b \sim 0.06$, or an opening angle of the winds of $(2b)^{1/2} \sim 20^\circ$ (8), producing an apparent luminosity $1/b$ higher than the intrinsic isotropic luminosity that they estimate being slightly above Eddington. Given the mass accretion rate we measure, the beaming factor inferred through the standard collimating wind argument they use would be $b \sim 73/\dot{m}^2 \approx 0.0023$, or an opening angle of $\sim 4^\circ$, which would produce an observed luminosity above ~ 400 times Eddington assuming that the luminosity from the neutron star is Eddington-limited.

Note, also, that the minimum inclination of the system from the mass function is 17° , corresponding to a donor mass of $100M_\odot$, and to get a donor below $20M_\odot$, the inclination needs to be $\geq 28^\circ$ (See Materials and Methods). With such a collimating wind, we would only see pulsations when the inner disk and its collimating wind have a large tilt by the same amount with respect to the orbit. The reported 60-day super-orbital modulation in the system (75), and the fact that pulsations are often not observed, might be interpreted in principle as a sign of the precession of such an inner disk structure; however, the relatively high fraction of time where pulsations *are* observed, including for ~ 20 straight days in 2014, shows that this occultation, if produced by a precessing occulting outflow with the properties predicted by the beaming models, should still happen in a range of observing angles which is lower than observed.

Therefore, we argue that the widely adopted formula to estimate beaming $b \sim 73/\dot{m}^2$ is not valid, at least for the case of accreting neutron stars such as M82 X-2.

Obs. ID	Epoch MJD	Energy keV	f_{spin} Hz	\dot{f}_{spin} 10^{-12} Hz/s
80002092002	56681.24439	8-30	0.728512(4)	$-70(140)$
80002092004	56683.80988	8-30	0.7285331(31)	110^{+140}_{-70}
80002092006	56688.80902	8-30	0.7285487(5)	$16(4)$
80002092007	56694.12258	3-30	0.7285613(8)	$34(10)$
80002092007	56697.38070	3-30	0.7285797(11)	$82(18)$
80002092008	56699.14063	3-30	0.728596(4)	$130(260)$
80002092009	56700.75316	3-30	0.7286097(12)	$101(22)$
80002092011	56720.87758	8-30	0.7287597(26)	$130(50)$
30101045002	57495.31180	8-30	0.7251913(15)	$-78(17)$
90201037002	57641.99852	8-30	0.723903(6)	$-120(240)$
30502021002	58919.09530	3-30	0.7219303(16)	$60(40)$
30602027002	59312.65086	3-30	0.7222100(20)	$90(60)$
30602027004	59326.05680	8-30	0.722294(4)	$60(130)$
30702012002	59505.27806	3-30	0.7208657(12)	-79^{+23}_{-45}

Table S1: Detected pulsations, once data are corrected by the orbital solution found in this paper. ObsIDs in bold are those corresponding to new detections from this paper. The energy range is the one where the pulsations are detected with the highest significance. Data from ObsID 80002092006 start after the glitch reported by B20 at MJD 56685.7 ObsID 80002092007 has a sudden change of frequency, probably another glitch, around MJD 56696, therefore we split the observation in two parts around that epoch.

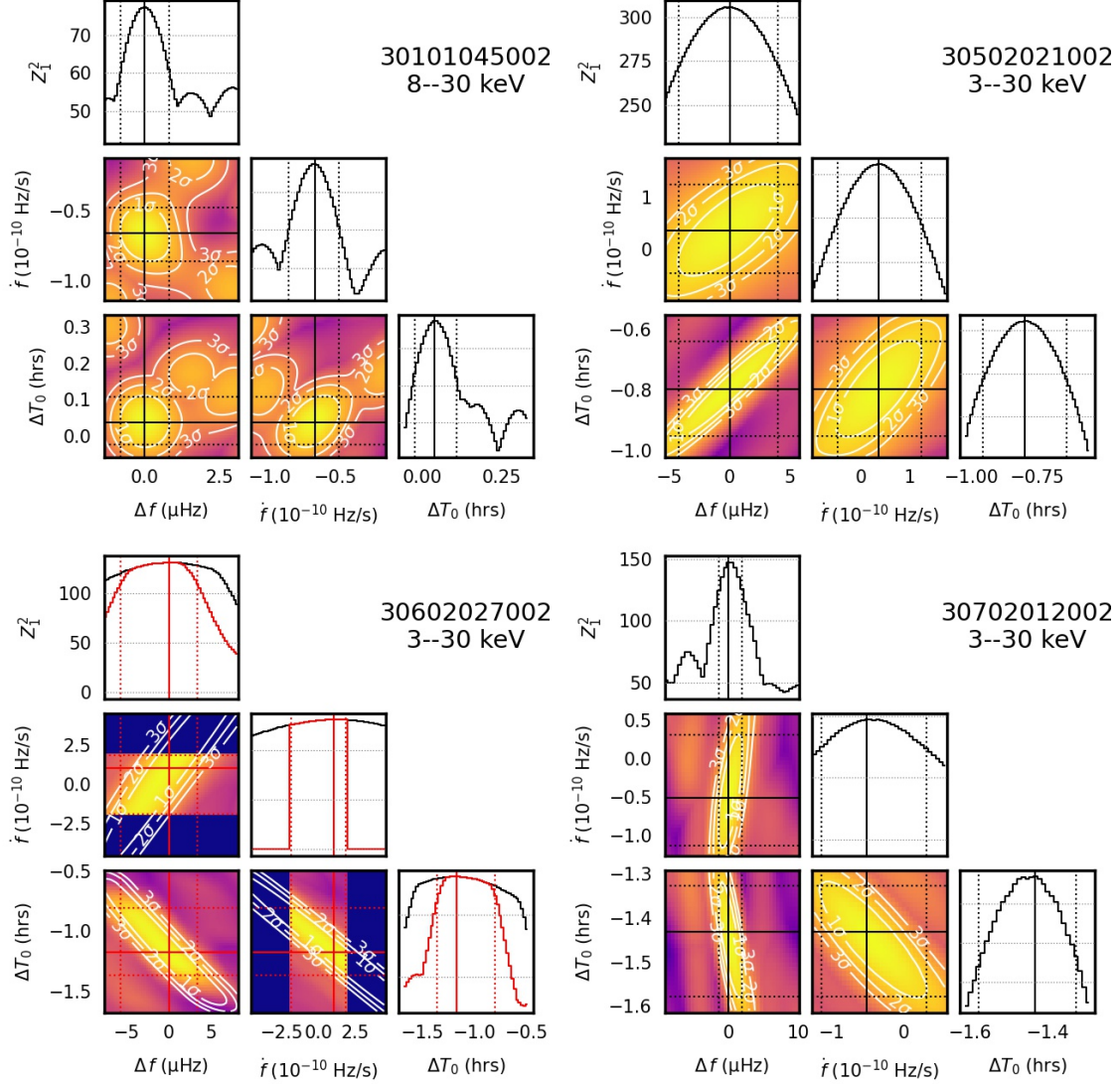


Figure S1: Detection of pulsations from ObsIDs 30101045002, 30502021002, 30602027002, and 30702012002. The color maps show the correlations between the spin-frequency, spin first derivative, and the drift of the periastron passage T_0 . The line plots show the statistics versus each parameter once all the others are marginalized. For the observations in the bottom plots, we set a hard limit at the allowed spin derivative, to plus/minus double the maximum spin derivative previously observed in this source. This, in turn, sets a hard constraint on the reasonable drift of T_0 . We plot the analysis in the energy range where the detection is stronger. When such a hard limit is in action, we plot the output curves in red.

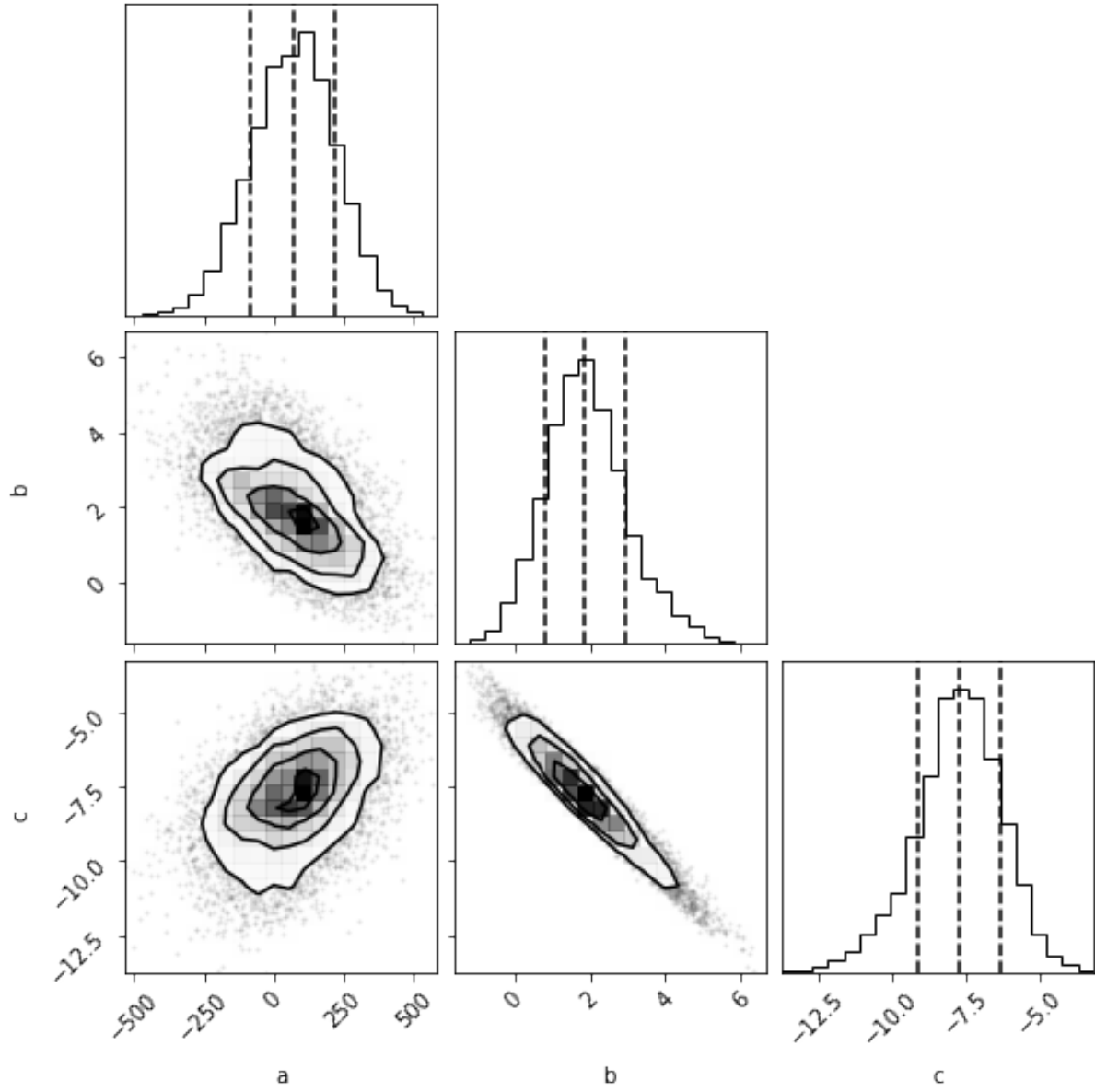


Figure S2: Corner plot of the posterior distribution of the parameters of the orbital decay with Equation 8, sampled with MCMC. Vertical dashed lines show the 16%, 50%, and 84% quantiles.

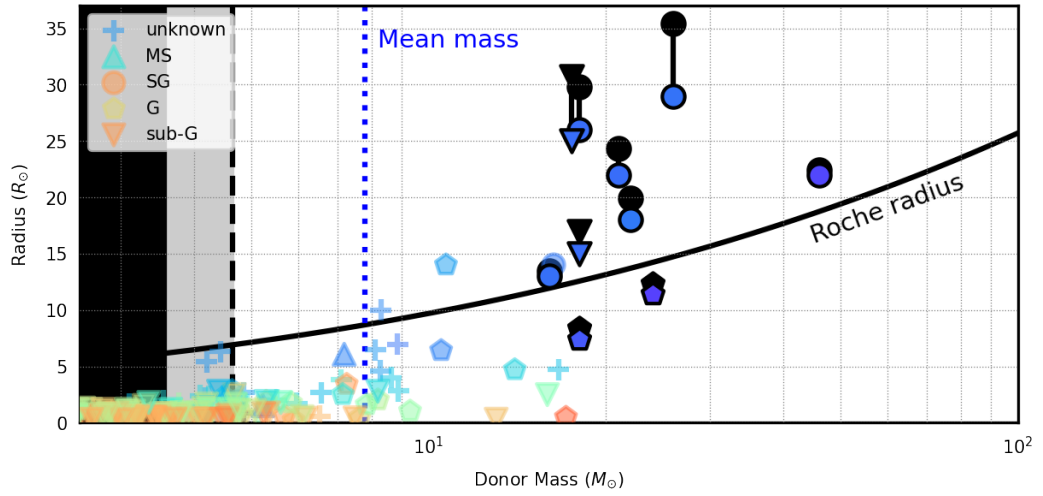


Figure S3: Roche Lobe radius in Eggleton approximation (76) versus mass for the donor star in M82 X-2. The donor has to lie around the black solid line in order to undergo Roche Lobe overflow. We overplot all donors from the HMXBs in (17) and all semidetached binary stars from (77) for comparison. For the HMXBs, we plot in black the Roche Lobe radius. Colors span the A (red)–O (blue) spectral types, and markers indicate different branches in the HR diagram. The grey shaded area is excluded by the absence of eclipses. The black area is prohibited by the mass function and the necessity that $\sin i \leq 1$.

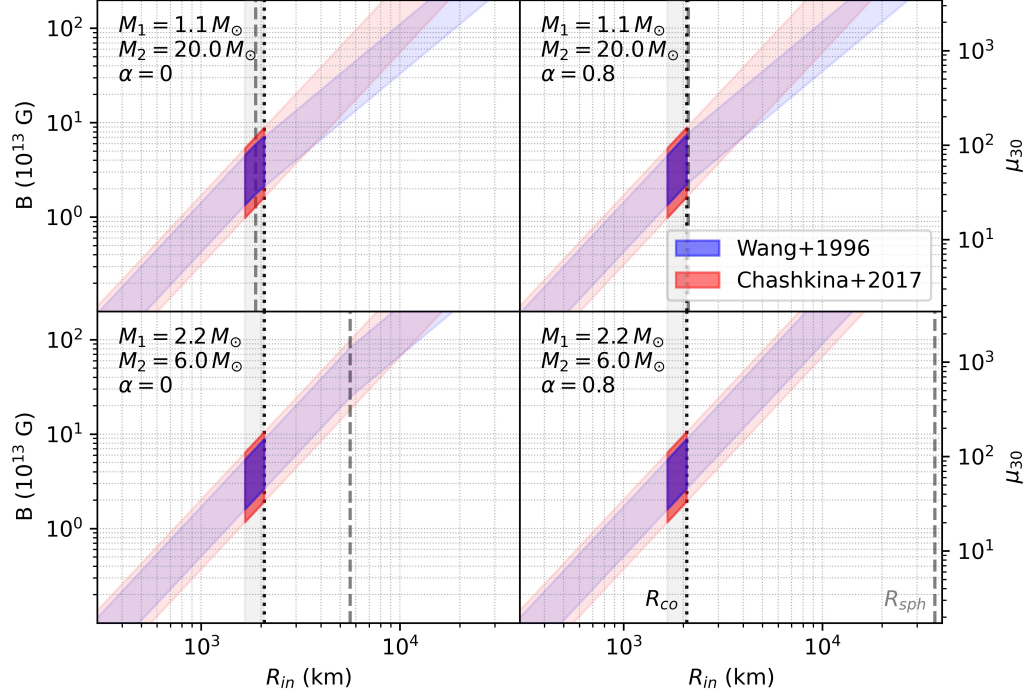


Figure S4: neutron star dipolar magnetic field estimate assuming spin equilibrium as described in the text, comparing the models from (28) (the area corresponds to values of $0.5 < \xi < 1$) and from (29) (the area covers the range of viscosity parameter $0.01 < \alpha_v < 0.3$), in four cases with a range of mass ratios and a different mass loss fraction (α in Equation 15) from the donor. We show R_{co} and R_{sph} with vertical lines. Note that a lower mass ratio increases the estimated mass transfer. Also, the mass loss from the donor implies a larger mass transfer rate to justify the observed derivative. This explains the larger R_{sph} . We highlight the region where $0.8 < R_{in}/R_{co} < 1$, as expected from spin equilibrium. For the traditional model we took into account a change of accretion rate due to mass loss inside R_{sph} . The estimated dipolar magnetic field is always above 10^{13} G for reasonable values of the parameters.